Powder Technology 316 (2017) 123–130

Contents lists available at ScienceDirect

Powder Technology

journal homepage: www.elsevier.com/locate/powtec

Experimental study of the application of rotating fluidized beds to particle separation

Justin M. Weber [a], Richard C. Stehle [b], Ronald W. Breault [a,*], Juray De Wilde [b,c]

[a] US Department of Energy's National Energy Technology Laboratory, 3610 Collins Ferry Road, Morgantown, WV 26505, United States
[b] Oak Ridge Institute for Science and Education, 3610 Collins Ferry Road, Morgantown, WV 26505, United States
[c] Materials and Process Engineering (IMAP), Université Catholique de Louvain, Place Sainte Barbe 2 (Réaumur building), 1348, Louvain-la-Neuve, Belgium

ARTICLE INFO

Article history:
Received 16 May 2016
Received in revised form 27 October 2016
Accepted 26 December 2016
Available online 28 December 2016

Keywords:
Fluidization
Rotating fluidized bed
Ash separation
Carbon capture
Chemical looping
Process intensification
High-G

ABSTRACT

Rotating fluidized beds provide a unique opportunity to exploit fluidization under higher particle forces. The centripetal force in a rotating fluid bed is typically on the order of 10 times the force of gravity. Since the force keeping the particles in the unit is larger, the drag force can also be larger, allowing for higher gas and slip velocities. This operating regime provides intensified gas-solids contact through higher mass transfer, heat transfer, gas throughput, and bubble suppression.

One application for using a rotating fluidized bed is in Chemical Looping Combustion (CLC). When solid fuels are used, oxygen carrier and ash are mixed in the process. In order to maintain high carbon capture efficiencies and recyclability of the oxygen carrier, the ash needs to be separated from the oxygen carrier. This separation can be done aerodynamically since the oxygen carrier is larger and heavier than the ash. It is theorized that rotating fluidized beds could improve both the gas-solid and solid-solid separation process efficiency and throughput as compared to conventional fluidized beds.

A 43 cm diameter, 2.5 cm long vortex chamber has been designed and constructed to investigate the application to particle separation. A series of experiments have been performed to investigate the separation of different binary mixtures of solids. These experiments demonstrate the use of a rotating fluidized bed for high-G intensified particle separation that can be combined with high-G intensified gas-solids contact and gas-solids separation.

Published by Elsevier B.V.

1. Introduction

In an effort to stabilize the global temperature increase to under 2 °C, the 2015 United Nations Climate Change Conference promoted an agreement to reduce carbon emissions from energy consumption. The U.S., which is the second largest consumer of energy at 15.5% of global energy demand, agreed to reduce carbon emissions by 27% by 2025 and cut power plant CO_2 pollution by 32% by 2030 based on 2005 levels [1]. In order to reduce carbon emissions while maintaining current energy capacity, efficient carbon capture systems need to be developed and deployed to reduce our carbon footprint while maintaining existing energy infrastructure.

When considering the electrical power sector, coal based power plants represent 40% of the electricity produced in the U.S. today [2]. The U.S. Department of Energy has set internal goals for carbon capture systems with 90% capture and less than a 35% increase in cost [3]. From the four main categories of CO_2 detailed by the DOE Advanced Carbon Dioxide Capture Program, chemical looping combustion (CLC) has been identified as having the lowest cost potential for simultaneous energy production and CO_2 separation [4].

1.1. Chemical looping combustion

In chemical looping combustion, the oxygen needed for reaction with a fuel source is supplied by an oxygen carrier that regenerates within the system. This allows for the combustion products to be controlled so as to consist primarily of CO_2 and steam where steam can be removed by condensation leaving a pure stream of CO_2. Metal oxides represent the oxygen carrier in most CLC systems where the oxide is chemically reduced by the fuel source and then re-oxidized under a stream of air exothermically to release energy in the form of heat [5,6]. There are a number of different CLC reaction processes that utilize a range of fuels, this study focusing on the combustion of coal [7,8]. The reaction steps below represent the global reaction involving coal, a metal oxide, and steam.

$$C + H_2O \leftrightarrow CO + H_2 \quad (1)$$

$$MeO_x + \delta CO + \delta H_2 \rightarrow MeO_{x-2\delta} + \delta CO_2 + \delta H_2O \quad (2)$$

* Corresponding author at: US DOE/NETL, PO Box 880, Morgantown, WV 26507, United States.
E-mail address: Ronald.breault@netl.doe.gov (R.W. Breault).

http://dx.doi.org/10.1016/j.powtec.2016.12.076
0032-5910/Published by Elsevier B.V.

$$MeO_{x-2\delta} + \delta O_2 \rightarrow MeO_x \quad (3)$$

The coal consists of solid carbon and hydrogen which is completely gasified by the supplied steam to produce a syngas of CO and H_2. The syngas reacts with the metal oxide present in the system to form a reduced metal oxide, CO_2, and steam. Effectively separating the CO_2 and steam from the reduced oxide then occurs by removing the gaseous species from the system. The reduced oxide then reacts with a supplied stream of air to return to its oxidized state as unconsumed air leaves the system. Fig. 1 illustrates this process and gives insight into the system layout.

Reaction 1 represents full conversion of carbon into CO, but in reality there will be partially converted carbon that remains with the produced syngas. This solid species will be present in low quantities with the oxygen carrier after the reduction step and will need to be separated prior to the carrier experiencing oxidation conditions. The rotating fluidized bed technology introduced in this report is intended to address the issue of solids separation of ash from the oxygen carrier.

1.2. Rotating fluidized bed

Rotating fluidized beds present a unique application to overcome performance limitations commonly associated with conventional fluidized bed technology. Rotating fluidized beds operate under high-G conditions which allow for gas-solid slip velocities to exceed the terminal velocity of a particle while maintaining a uniformly dense particle bed [9]. The particles remain entrained within the bed due to a centrifugal force that radially forces the particles outward. The process gas is fed tangentially through multiple slots positioned around the outer cylindrical wall as seen in Fig. 2. The gas is then deflected inward as it comes into contact with particles and leaves through a center outlet or chimney. Due to the gas traveling radially inward, drag forces on the particles are present counteracting the centrifugal forces. Careful design and implementation is needed when addressing these competing forces to ensure entrainment is maintained and particles do not exit out the chimney. The centrifugal forces and gas-solid drag forces are both dependent upon gas velocities and particle properties, so the design of the inlet slots around the outer ring becomes a critical parameter. It has been previously studied that tangential momentum for a given gas flow rate increases as gas inlet slots are decreased in size or number [10]. However a minimum number of slots are required in order to ensure bed uniformity and the slot size cannot be smaller than the particle diameter. Likewise, experimental results showed that as particle size or density is decreased, slot size needed to be decreased in order to guarantee solids retention.

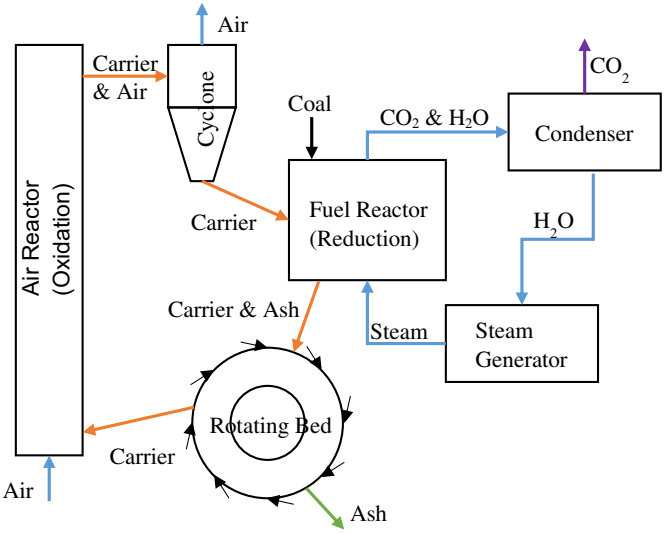

Fig. 1. Layout of a chemical looping reactor system implemented for ash separation.

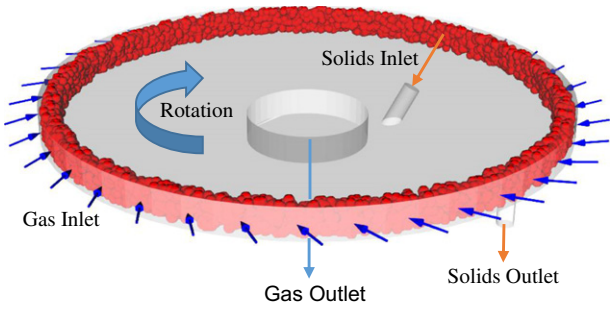

Fig. 2. Vortex chamber depiction for rotating fluid bed generation.

What previous studies with rotating beds have shown is the potential of this technology to impact a number of different applications such as biomass drying, gas adsorption processes, and solid-solid separation [11]. Due to the driving forces, particle size and density impact how the bed is developed within the rotating bed. The centrifugal forces on a denser species are greater allowing for a bed of mixed particles to separate within the rotating bed. Similarly, drag forces are greater for larger particles resulting in separation between different size particles. Due to high-G operation, ash is expected to separate effectively from an oxygen carrier like a metal oxide in a rotating fluidized bed and can then be extracted to allow for near complete separation of the two species.

2. Experimental apparatus

The rotating fluidized bed vortex chamber consists of a 43 cm diameter, 2.5 cm long vortex chamber which was 3D printed out of nylon, Fig. 3. The air distributor has 38, 381 μm wide slots equally spaced and angled at 16° relative to the tangent at the slot location.

The distributor is bounded by a 1.27 cm thick clear acrylic top plate and a steel bottom plate. The chamber stack is positioned by steel supports and can be suspended in a vertical or horizontal position. Fig. 4 details the vortex chamber design. Air enters at four locations through the bottom plate and passes across the distributor ring into the main vortex region. The air exits the chamber through a 10.2 cm diameter chimney, also positioned on the bottom plate. A solids diverter plate, suspended 3 mm from the bottom plate, 40.6 cm in diameter, is used to prevent significant gas from exiting the solids outlet pipe.

The chimney-to-vortex chamber diameter ratio (D_c/D_{vc} where D_c is the diameter of the chimney and D_{vc} is the diameter of the vortex chamber) is 0.24, the vortex chamber length-to-diameter ratio (L/D_{vc} where L

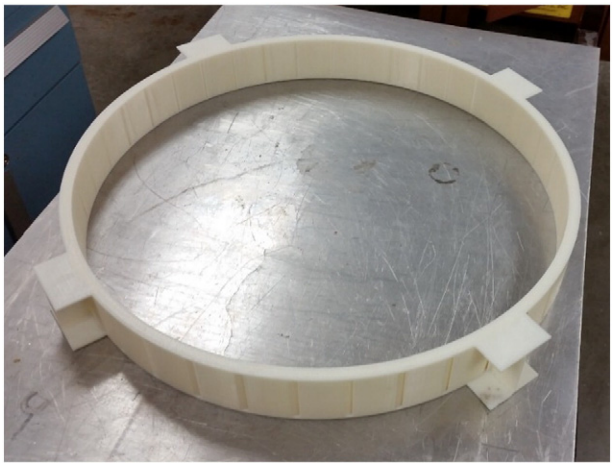

Fig. 3. 3-D printed vortex chamber.

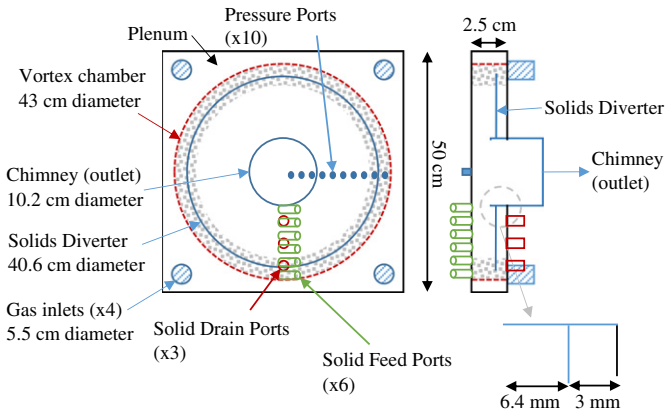

Fig. 4. Complete vortex chamber sizing.

is the length, or thickness of the vortex chamber) is 0.06. Optimal ranges $0.3 < D_c/D_{vc} < 0.5$ and $L/D_{vc} < 0.5$ were reported by Kochetov et al., but based on experiments with relatively large particles only [11]. The fraction of the chamber circumference taken by the gas inlet slots, λ, is 0.011, well below the upper limit reported by Kochetov et al. [11]. This λ is one of the design parameters that allows adjusting of the centrifugal force-to-radial gas-solid drag force ratio that will be experienced by the particles, effecting the bed density, uniformity and eventual solids losses via the chimney. For optimal bed uniformity, a high number of gas inlet slots is needed, but with fine particles λ must be sufficiently small [12]. To reduce λ, the slot size is preferentially decreased, but slot sizes significantly smaller than the particle diameter are not recommended as this leads to inefficient gas-solid momentum transfer in the vicinity of the gas inlet slots. In the present study, the slot size was 381 μm, about half the diameter of the larger particles used and about the size of the smaller particles. To achieve uniform operation 38 slots were used.

To keep the particle bed of given mass rotating at a given speed and compensate for shear with the wall, an estimate of the required gas flow rate can be made by knowing the amount of time the bed keeps rotating after abruptly stopping the gas supply. Considering, for example, a 3.5 cm thick bed (t_b) of HDPE with a solids volume fraction (ε_s) of 0.5 in the vortex chamber as described above, containing about 1 kg of particles and rotating at a tangential velocity ($v_{g,t}$) of 5 m/s, a typical value found in the literature [12]. If the bed keeps rotating for 1 s when the gas flow is stopped, the gas must supply tangential momentum (Δp_t) at a rate of 5 kg·m/s^2 to keep the bed rotating at the given speed. The required gas flow rate (Q_{in}) can then be calculated by:

$$\Delta p_t = Q_{in}\rho_g v_{g,t} \tag{4}$$

With the gas inlet velocity ($v_{g,in}$) given by:

$$v_{g,in} = \frac{Q_{in}}{nsH} \tag{5}$$

Where n is the number of slots, s is the width of the slots, and H is the thickness of the vortex chamber. A gas flow rate requirement (Q_{in}) of 140 m^3/h is found, corresponding to a gas injection velocity ($v_{g,in}$) of 107 m/s. A lower gas flow rate could not keep rotating the given bed at 5 m/s. Note that the gas phase residence time in the bed ($\tau_{res,g}$) can be calculated by:

$$\tau_{res,g} = \frac{t_b}{v_{g,r}} \tag{6}$$

Where $v_{g,r}$ is the gas velocity in the radial direction, which in the example is 0.015 s.

The acrylic top plate allows for visual inspection of the system in operation as well as imaging analysis. Inlet ports are positioned at different radial positions through the acrylic plate to allow for controlled solids feeding into the bed. The six solids feed ports are aligned tangentially (with the bed rotation) with a 45° angle downward, positioned at the following radii; 7.5, 9.9, 12.5, 15, 17.5, and 20 cm. For the tests described here, the solids were fed at a radius of 9.9 cm. Solids can be drained through the bottom plate by exit ports at the same angular position as the feed ports. The drain ports are located at the following radii; 10.2, 15.2, and 20.3 cm. For the tests described here, the solids were drained at a radius of 20.3 cm. Pressure tap locations are also positioned at different radial positions along the acrylic plate to accommodate pressure transducers for pressure drop readings. The solids inlet and exit ports are 1.27 cm in diameter with the pressure taps being 0.64 cm diameter.

The complete system layout is depicted in Fig. 5 and illustrates the desired operation of the rotating bed. Downstream of the chimney and solids outlets are collection filters. Upstream, air flow is controlled by a mass flow controller and is limited to 103 kPa . Solids are fed using a KTron screw feeder that controls the solids feed rate. The solids are driven into the inlet of the vortex chamber by air passing through an eductor. The solids outlet is controlled with a ball valve.

3. Material properties

Three materials were used in these experiments including phosphorescent high density polyethylene (HDPE), glass beads (GB), and cork. Particle sauter mean diameters (d_{SMD}), mean diameters (d_{50}), and sphericity were measured using a Sympatec QICPIC. Particle diameters ranged from 329 to 871 μm. Particle sphericities ranged from 0.8 to 0.92. The particle densities were measured using a helium Pycnometer and ranged from 0.19 to 2.51 g/cm^3. Minimum fluidization velocity, U_{mf}, was measured experimentally in a 6.35 cm diameter fluidized bed and ranged from 9.37 to 17.4 cm/s. The average single particle mass was calculated by:

$$m_p = \frac{4}{3}\pi r_p^3 \rho_p \tag{7}$$

Where r_p is the radius of the particle ($\frac{d_{50}}{2}$) and ρ_p is the particle density. The single particle mass varied from 0.047 to 0.298 mg. These properties are detailed in Table 1.

When considering the forces that will drive separation in a developed bed within the vortex chamber, centrifugal forces and drag forces act in opposite directions to one another in the radial direction. For a bed of two species with different particle density, the heavier species will experience higher centrifugal forces. This will promote the location of the heavier species to be at a radial position further from the center of the vortex chamber than that of a lighter species. Table 1 shows that HDPE to be 5 to 6 times larger in mass than that of both glass and cork. As the heavier particle, HDPE should separate from either species

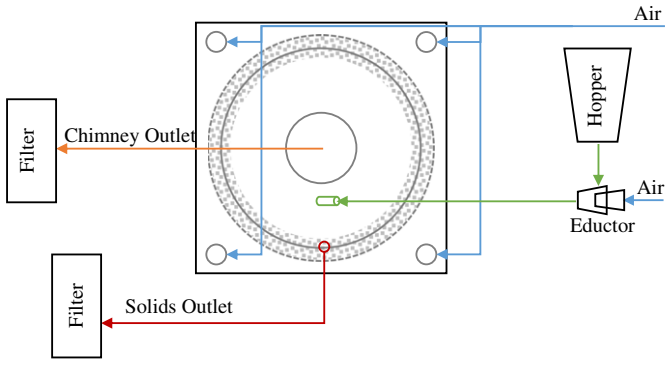

Fig. 5. Experimental system layout.

Table 1
Particle properties.

Material	Density	d_{SMD}	d_{50}	Sphericity	U_{mf}	Particle mass
	g/cm^3	μm	μm		cm/s	mg
High density polyethylene	0.86	871	885	0.92	17.4	0.312
Glass beads	2.51	329	333	0.92	9.47	0.049
Cork	0.19	797	835	0.8	9.37	0.058

within a developed bed toward the exterior of the chamber. Drag forces will drive particles of larger diameter toward the center of the chamber allowing for a secondary dependence on separation. Referring to Table 1, the glass beads have the smallest particle diameter, limiting the effect of drag on the glass particles when compared to the larger HDPE and cork particles which have similar particle sizes.

HDPE will be used to represent the carrier during operation of the vortex chamber with cork representing the properties of ash. Due to the larger centrifugal forces on HDPE and similar drag forces present on both species, it is assumed separation will occur with HDPE particles entrained within the developed bed toward the exterior of the chamber and cork particles located closer to the center. It is possible for the cork particles to elutriate out of the chamber through the chimney due to the large drag forces present.

Glass beads will be supplied with HDPE in separate runs in the absence of cork as a secondary means of investigation. Due to the low drag and centrifugal forces on the glass beads it is unclear if separation will occur since HDPE will experience larger forces in both directions in comparison.

4. Results and discussion

4.1. Fluidization behavior with HDPE particles

While feeding HDPE into an initially empty vortex chamber, a slugging phenomenon was observed at low solids inventories. A significant amount of the inventory grouped together into a mass of solids on one side of the chamber, which continued to rotate around as seen in Fig. 6. The imbalance in the inventory caused by the slug induced significant vibrations in the apparatus.

By analyzing the video, a slugging frequency can be extracted by looking at the average intensity of pixels located near the wall of the vortex chamber. A video was recorded at a resolution of 1920 × 1080 pixel at a frame rate of 29.88 frames/s for a total video length of 20 s. The interrogation window depicted by the red box in Fig. 6 was from 1100 to 1400 pixels in the x direction and 750 to 900 pixels in the y direction. The red channel of the color video was most sensitive to the difference between the solids and the vortex chamber.

The resulting signal on the left side of Fig. 7 has a low frequency component, attributed to movement of the camera, as well as a higher frequency component which is caused by the slug passing through the interrogation window. The higher intensity values of the high frequency signal correspond to the slug.

Performing a Fast Fourier Transform on the average pixel intensity, with no filtering or averaging, a strong peak at 6.9 Hz is present in the plot on the right side of Fig. 7. This frequency compares well to the observed frequency. If the assumption is made that the solids are moving as a solid body [12], a solids velocity can be estimated by Eq. (8). Unfortunately, the video quality and speed is not good enough to verify this assumption or determine if the solids angular velocity changes with radius.

$$\omega = 2\pi f \tag{8}$$

Where ω is the angular velocity and f is the frequency in revolutions/s. At a frequency of 6.9 Hz, this results in an angular velocity of 43 rad/s. With a radius of 21.5 cm, the particles are moving at a tangential speed of 9.3 m/s.

For reference, at a volumetric flow rate of 14 m^3/min, the gas velocity through the slots, as calculated by Eq. (5) is approximately 331 m/s. The radial component of the gas velocity, discussed further in Section 4.4, ranges from 7 to 30 m/s, depending on the radius.

The centripetal acceleration, a_c can be calculated with:

$$a_c = \frac{{v_{p,t}}^2}{r} \tag{9}$$

Where $v_{p,t}$ is the tangential speed and r is radius. During this condition, the particles were experiencing a centripetal acceleration of 41 G, or 41 times the acceleration due to gravity on earth.

As solids were continually added to the bed, a critical bed mass was achieved were the slugging phenomenon ceased and a uniform bed was observed, Fig. 8, confirming observations by other groups [12]. Vibrations and audible noise reduced significantly, as well as the pressure drop over the chamber. This bed stayed uniform over a wide range of flow rates. The critical mass could not be measured due to inconsistencies with the solids feeding.

4.2. High density polyethylene and cork

A 50% HDPE, 50% cork mixture by weight was fed into the rotating fluid bed at about 0.2 kg/min. Gas flow rate to the bed was sustained at 14 m^3/min. During this test, large amounts of the cork, with very little HDPE, exited through the chimney of the unit as expected due to greater effect of the drag force. The HDPE stayed inside the chamber and a bed was formed with the remaining cork. Slugging of the bed was observed at low solids inventory, however as the inventory was increased, the slugging stopped and a stable uniform bed was observed. Fig. 9 shows a picture of the slug. There seemed to be a segregation of the remaining cork from the HDPE, with the HDPE seen in greater quantity at the outer wall of the chamber.

Feeding of solids into the bed was problematic due to the eductor not providing a large enough pressure gain to overcome the pressure inside the unit, despite using a solids feed port located close to the vortex

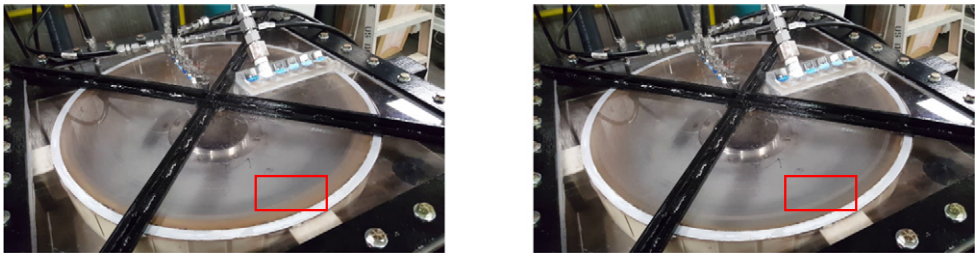

Fig. 6. Image of the slugging phenomenon. Slug at the front of the chamber (left), and slug at the back of the chamber (right). The red box on both images represents the Interrogation window used in the video analysis.

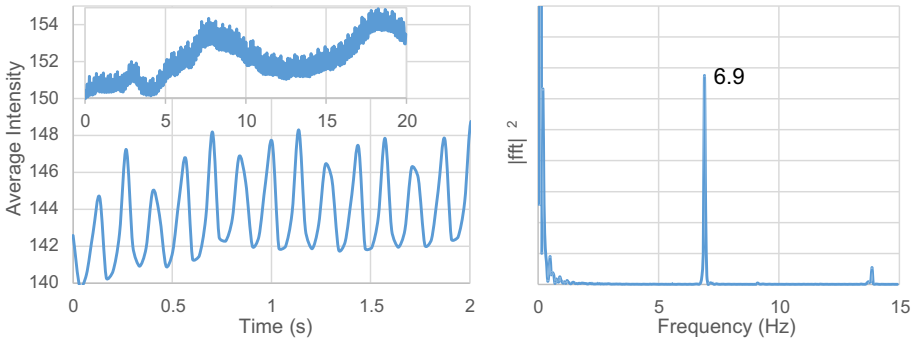

Fig. 7. Average pixel intensity for the interrogation window over the first 2 s, all 20 s displayed in the inset (left) and the power spectrum of the signal (right).

chamber central axis where the pressure is lower. The amount of mass successfully fed into the unit was unknown. From observation of the bed, the bed height (radial thickness) was on the order of 3 to 4 cm.

Once the solids had been fed into the unit and a bed was maintained for an extended period of time, the solids outlet at the outer most radial position was opened. A continuous stream of primarily HDPE with low amounts of cork was observed with minimal gas exiting. In order to quantify the separation efficiency, samples of the solids fed into the system, solids that exited through the chimney, and solids that were drained through the solids outlet where collected. These solids samples were then analyzed by taking two photos of the material on a black piece of paper. The image on the left in Fig. 10 was taken with ambient lighting. The image on the right in Fig. 10 was taken with no ambient lighting (the setup was enclosed in a cardboard box) just after the HDPE was charged with a 250 W halogen lamp.

The first, ambient light, image was thresholded to segment all the particles from the background. The red channel of the color image was more sensitive to the particles then the other two channels. Pixel values of the red channel that were higher than 70 to 120, depending on the specific lightning conditions, were tagged as particle pixels.

The second, no ambient light, image was thresholded to segment just the HDPE since only the HDPE phosphoresces. The green channel of the color image was more sensitive to the phosphorescence then the other two channels. Pixel values of the green channel that were higher than 10 to 30, depending on the lighting, were tagged as high density polyethylene particles. The first image, the green channel of the second image, and the first image with the tagged pixels of all the particles and just the HDPE, for all three samples can be seen in Fig. 11.

The quantitative particle counts from the images were consistent with the observations from the experiment. At the equivalent feed rate by mass, the heavier HDPE only represented 20% of the total solid particle count entering the bed. The solids that exited out of the chimney and collected in the downstream filter was 98% cork. Through the drain port, the mixture was 55% HDPE, 45% cork. Due to the placement of the outer most drain port, both portions of the segregated bed drained.

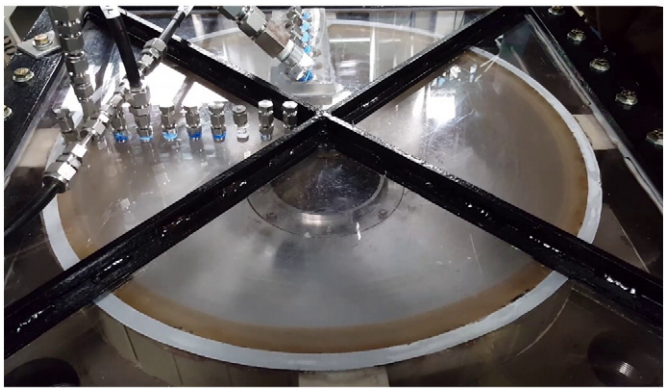

Fig. 8. Stable and uniform bed developed after the critical mass is reached.

In future tests, a larger or thicker bed will need to be developed so as to allow for draining from one section of the bed can occur. In addition, the weight scales will be utilized at the downstream collection locations to obtain mass approximations for the captured particles.

The results do show that separation can be achieved quickly within a thin bed as compared to conventional segregation in fluid bed approaches. This leads to process intensification, allowing for smaller systems.

4.3. High density polyethylene and glass beads

A mixture of 50% glass beads, 50% HDPE by weight was fed into the unit at flow rate of about 0.2 kg/min. Gas flow rate to the bed was sustained at 14 m^3/min. A well-defined bed was developed and very few particles escaped through the chimney during operation. Visually separation could not be seen during testing within the bed or at the solids outlet. The dependence on drag and centrifugal forces for these two species were counteracted as explained in the previous section. Glass beads experienced low drag and low centrifugal forces while HDPE in comparison experienced high drag and high centrifugal forces. Due to this relation, glass beads did not segregate or separate from the HDPE.

4.4. Drag compared to centripetal force

The determination of whether a particle stays inside the vortex chamber or exits through the outlet depends on whether the centripetal force or the drag force in the radially inward direction is greater. First the situation is analyzed after the first particles enter the vortex chamber and no bed is present yet (the void fraction, ϵ, is 1.0). Assuming uniform flow across the distributor and not accounting for the effects of the end walls, the superficial radial gas velocity ($v_{g,r}(r)$) within the vortex chamber can be estimated based on radial position:

$$v_{g,r}(r) = \frac{Q_{in}}{2\pi r L} \tag{10}$$

Where Q_{in} is the volumetric gas flow rate and L is the vortex chamber length (2.5 cm in this case). As the cross-sectional area decreases with decreasing radius, the superficial gas velocity has to increase, Fig. 12.

The determination of the superficial radial gas velocity allows for the estimation of the drag force in the radial direction ($F_d(r)$) on individual particles. If the assumption is made that the particles can be treated as spheres, the drag force in the radial direction for a single particle can be estimated by:

$$F_d(r) = \frac{1}{2}\rho_g v_{g,r}^2 C_D(r) A_p \tag{11}$$

Fig. 9. "Snapshot" of a slug during low solids inventory. The solids are moving from right to left. A segregation of the cork (inner bed) and HDPE (outer bed) is observed.

Where ρ_g is the density of air, $C_D(r)$ is the drag coefficient as a function of radius, and A_p is the cross-sectional area of a particle. The drag coefficient can be determined by [13]:

$$C_D(r) = \frac{24}{Re} + \frac{2.6\left(\frac{Re}{5.0}\right)}{1+\left(\frac{Re}{5.0}\right)^{1.52}} + \frac{0.441\left(\frac{Re}{263{,}000}\right)^{-7.94}}{1+\left(\frac{Re}{263{,}000}\right)^{-8.00}} + \left(\frac{Re^{0.80}}{461{,}000}\right) \quad (12)$$

Where Re is the particle Reynolds number expressed as:

$$Re = \frac{\rho_g d_p v_{g,r}}{\mu_g} \quad (13)$$

The centripetal force ($F_c(r)$) can also be estimated as a function of the radius by assuming that the particle angular velocity remains constant over the radius and assuming uniformity over the entire length of the vortex chamber, i.e. neglecting the effects of the end walls:

$$F_c(r) = m_p r \omega^2 \quad (14)$$

where m_p is the mass of a particle and ω is the angular velocity. The resultant values are plotted in Fig. 13 for each of the three materials used in the vortex chamber and using the measured typical particle rotation speed, assumed to be independent of the solids loading to facilitate the analysis.

Fig. 13 explains the efficient separation of HDPE and Cork with the given vortex chamber and operating conditions, as well as the poor separation of HDPE and GB. The radius at which the drag force ($F_d(r)$) equals the centripetal force ($F_c(r)$) is indeed almost the same (8.78 cm compared to 9.18 cm for the HDPE, and GB respectively). This means that there is no gas velocity that could be run to separate the two materials. However, the radius at which the drag force ($F_d(r)$) equals the centripetal force ($F_c(r)$) for the cork is at a much larger radius then the HDPE (15.48 cm). This allows the cork to be easily separated from the HDPE. Following the same reasoning, the glass beads and the cork should also separate easily. Accounting for the radial position of the solids feeding port that was used, Fig. 13 also explains the immediate loss of Cork particles into the chimney after being fed into the chamber.

Fig. 14 repeats the analysis in the presence of a particle bed. In the particle bed region, the radial gas velocity, $v_{g,r}(r,\varepsilon)$, can be calculated from:

$$v_{g,r} r, \epsilon = \frac{v_{g,r}(r)}{\epsilon} \quad (15)$$

where ϵ is the bed void fraction. Considering that there is a 3 cm thick bed with a void fraction of 0.6, Fig. 14 shows that also in the particle bed region the drag force on the cork is larger than the centripetal force, explaining the cork exiting the vortex chamber.

5. Conclusion

A rotating fluidized bed was designed and constructed to experimentally determine if it could be used to separate a binary mixture of granular materials. Results showed that two distinct materials could be separated within the chamber based upon their particle size and mass. Making a series of assumptions, the drag force in the radial direction and centripetal force can be estimated for the particles. Once the drag force is larger than the centripetal force, the particle will leave the vortex chamber. In order for solid-solid separation to occur, the radial location at which the drag force in the radial direction and the centripetal force are equal has to be significantly different. This also affects the required particle feed location.

To further analyze the designed system for practical application development, continuation of this study is planned to show how two separated species within the bed can be maintained and then collected. Design alterations are being considered to address concerns on

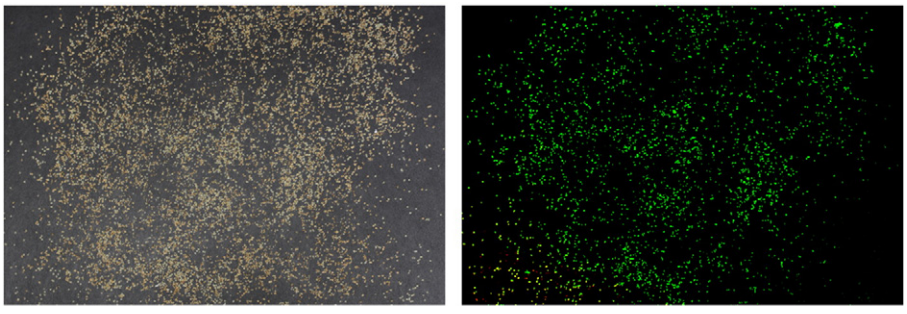

Fig. 10. The two photos taken for each sample. Ambient lighting (left) and no ambient lighting just after the high density polyethylene was charged (right).

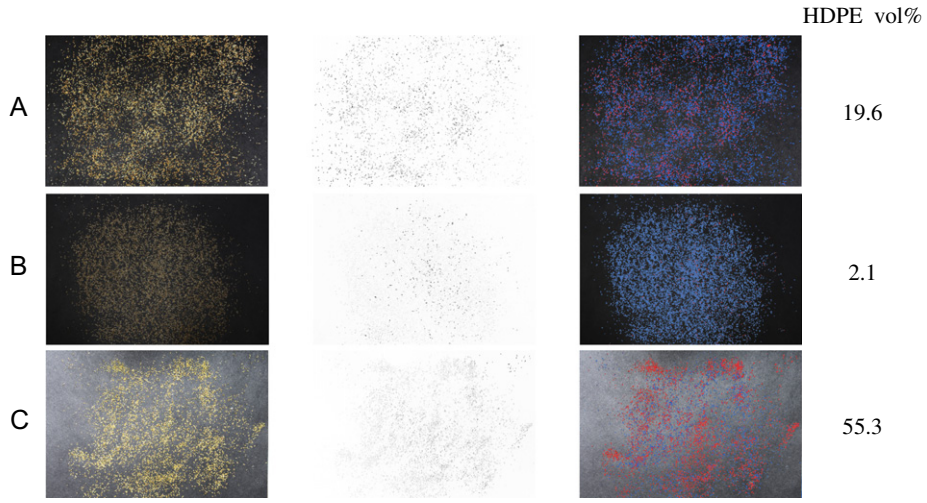

Fig. 11. From top to bottom; A) High density polyethylene and cork feed mixture, B) Solids exiting the chimney, and C) Solids exiting the solids outlet (from left to right; original image, green channel of fluoresced particles, and original image with tagged particles).

controlling material inventory in the chamber as well as leaving the bed for collection. HDPE, as an analog material for iron oxide in a chemical looping combustion process, will be used in future studies along with a range of ash analog materials that include cork. Imaging techniques using high speed video are currently being implemented to give increased visual clarity within the bed during operation as well as extracting accurate particle velocity measurements.

The continued investigation of this technology and identification of process applications will hopefully lead to process intensification, allowing for more compact reaction systems as opposed to conventional reactors such as circulating fluidized bed and fluid bed reactors.

Notation

a_c	centripetal acceleration, m/s^2
A_p	cross-sectional area of a particle, $\frac{\pi d_p^2}{4}$, m^2
C_D	coefficient of drag
D_c	Diameter of the chimney, 10.2 cm, m
D_{vc}	Diameter of the vortex chamber, 43 cm, m
d_p	particle diameter, m
d_{50}	mean particle diameter, m
d_{SMD}	sauter mean diameter, m
F_d	drag force on a single particle, N
F_c	centripetal force, N
G	acceleration due to gravity, m/s^2
L	vortex chamber length (thickness), 2.5 cm, m
m_p	mass of a particle, kg
n	number of slots, 38
Q_{in}	volumetric gas flow rate, m^3/s
Re	particle Reynolds number
r	vortex chamber radius, m
r_p	radius of a particle, m
s	width of a slot, 381 μm, m
t_b	thickness of the bed, m
$v_{g,r}$	velocity of gas in the radial direction, m/s
$v_{g,t}$	velocity of gas in the tangential direction, m/s
$v_{g,in}$	velocity of gas through a slot, m/s
$v_{p,t}$	velocity of particles in the tangential direction, m/s
Δp_t	change in the tangential momentum of the solids, kg·m/s^2
ϵ	void fraction
ε_s	solids fraction
λ	fraction of the chamber circumference taken by the gas inlet slots
μ_g	gas viscosity, Pa·s
ρ_g	gas density, kg/m^3
ρ_p	particle density, kg/m^3
$\tau_{res,g}$	gas residence time in the bed, s
ω	angular velocity, rad/s

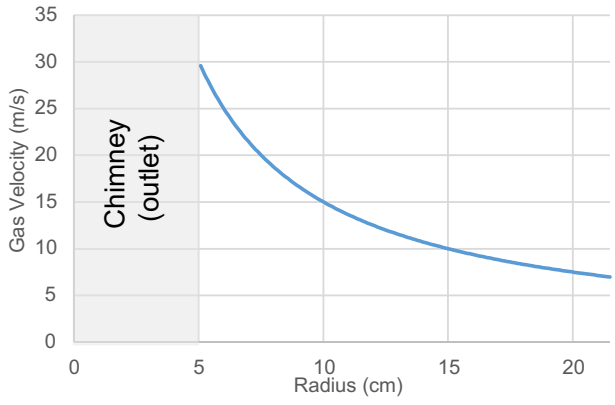

Fig. 12. Radial air velocity within the vortex chamber with respect to radial position in the absence of a particle bed.

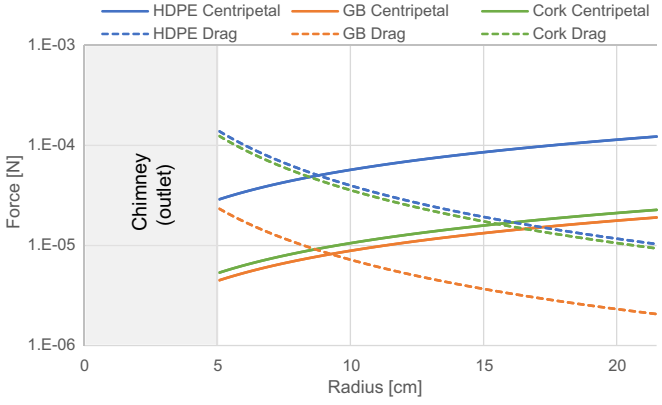

Fig. 13. Comparison of drag forces and centripetal forces on individual particles within the vortex chamber for each material in the absence of a particle bed (initial particle feeding).

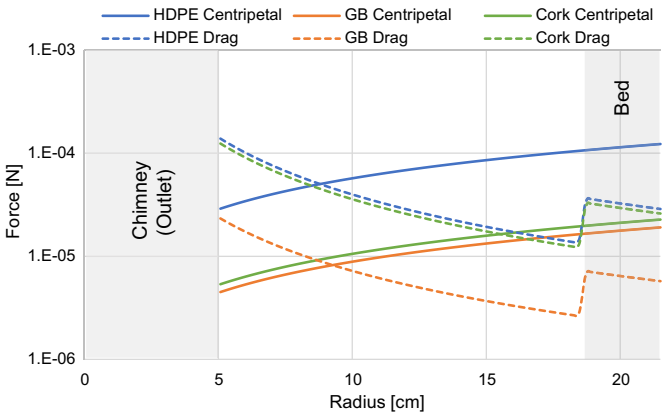

Fig. 14. Comparison of drag forces and centripetal forces on individual particles within the vortex chamber for each material after building up a particle bed with void fraction 0.6.

Disclaimer

This project was funded by the Department of Energy, National Energy Technology Laboratory, an agency of the United States Government, through a support contract with URS Energy & Construction, Inc. Neither the United States Government nor any agency thereof, nor any of their employees, nor URS Energy & Construction, Inc., nor any of their employees, makes any warranty, expressed or implied, or assumes any legal liability or responsibility for the accuracy, completeness, or usefulness of any information, apparatus, product, or process disclosed, or represents that its use would not infringe privately owned rights. Reference herein to any specific commercial product, process, or service by trade name, trademark, manufacturer, or otherwise, does not necessarily constitute or imply its endorsement, recommendation, or favoring by the United States Government or any agency thereof. The views and opinions of authors expressed herein do not necessarily state or reflect those of the United States Government or any agency thereof.

Acknowledgements

The authors would like to acknowledge the financial and technical support of DOE's Advanced Combustion Program. This research was supported in part by an appointment to the National Energy Technology Laboratory Research Participation Program, sponsored by the U.S. Department of Energy and administered by the Oak Ridge Institute for Science and Education. J. D.W. would like to thank Dr. Bhima Sastri (U.S. Department of Energy, HQ) for his help in organizing this research collaboration and follow-up of the project.

References

[1] United Nations Framework Convention on Climate Change, Conference of the Parties 21st Session, 2015 (FCC/CP/2015/L.9/Rev.1).
[2] U.S. Energy Information Administration, Monthly Energy Review, February 2016 (DOE/EIA-0035(2016/02).
[3] U.S. Department of Energy, National Energy Technology Laboratory, Carbon Dioxide Capture R&D Program: Technology Update, May 2015.
[4] R.W. Breault, E.D. Huckaby, Parametric behavior of a CO_2 capture process: CFD simulation of solid-sorbent CO_2 absorption in a riser, Appl. Energy 112 (2013) 224–234.
[5] R. Porrazzo, G. White, R. Ocone, Fuel reactor modelling for chemical looping combustion: from micro-scale to macro-scale, Fuel 175 (2016) 87–98.
[6] A. Cabello, P. Gayan, F. Garcia-Labiano, L.F. de Diego, A. Abad, J. Adanez, On the attrition of oxygen carriers in chemical looping combustion, Fuel Process. Technol. 148 (2016) 188–197.
[7] R.W. Breault, E.R. Monazam, J.T. Carpenter, Analysis of hematite re-oxidation in chemical looping process, Appl. Energy 157 (2015) 174–182.
[8] E.R. Monazam, R.W. Breault, R. Siriwardane, Reduction of hematite (Fe_2O_3) to wustite (FeO) by carbon monoxide (CO) for chemical looping combustion, Chem. Eng. J. 242 (2014) 204–210.
[9] P. Eliaers, J.R. Pati, S. Dutta, J. De Wilde, Modeling and simulation of biomass drying in vortex chambers, Chem. Eng. Sci. 123 (2015) 648–664.
[10] P. Eliaers, A. de Broqueville, A. Poortinga, T. van Hengstum, J. De Wilde, Powder Technol. 258 (2014) 242–251.
[11] L.M. Kochetov, B.S. Sazhin, E.A. Karlik, Hydrodynamics and heat exchange in vortex drying chambers, Invest. Calculation Thermochem. Processes 9 (1969) 10–11.
[12] J. De Wilde, Gas-solids fluidized beds in vortex chambers, Chem. Eng. Process. 85 (2014) 256–290.
[13] F.A. Morrison, An Introduction to Fluid Mechanics, Cambridge University Press, New York, 2013 625.